




# *In operando* neutron imaging characterizations of all-solid-state batteries

Daxian Cao,\* Yuxuan Zhang, Tongtai Ji, and Hongli Zhu\* 

The surge in electric vehicle demand has propagated the extensive application of lithium-ion batteries (LIBs) in recent years. Gaining significant traction due to their promising high-energy density and elevated safety over traditional LIBs, all-solid-state Li batteries (ASLBs) have nonetheless been faced with hurdles relating to battery performance. These include concerns with interfacial compatibility, structural stability, Li dendrite inhibition, and large-scale manufacturing. To tackle these issues, it is necessary to employ advanced characterization methods to comprehend the intrinsic mechanisms within ASLBs. In this article, we advocate for the use of neutron imaging as a nondestructive approach for the *operando* visualization of ASLBs. We draw comparisons with other *operando* visualization strategies, underline the benefits of neutron imaging, and discuss its potential applicability in the scrutiny of all-solid-state Li metal batteries and all-solid-state Li-sulfur batteries. Neutron imaging provides valuable insights into the dynamics of Li concentration, reaction mechanisms, and transport constraints in ASLBs. These insights are pivotal in contributing to the evolution of high-performance all-solid-state batteries.

## Introduction

The ever-increasing need for electric vehicles (EVs) in the global market triggered the burst of lithium-ion batteries (LIBs) over the past decades.<sup>1,2</sup> All-solid-state Li batteries (ASLBs), recommended for delivering high-energy density and safety simultaneously, received intense interest from both academia and industry.<sup>3</sup> Getting rid of using flammable liquid electrolytes, ASLBs contribute to outstanding safety.<sup>4</sup> More impressively, ASLBs promise an energy density of more than 500 Wh kg<sup>-1</sup>, surpassing the conventional LIBs, when coupled with high-energy electrodes, such as high-nickel oxide cathodes, sulfur cathode, Li metal anode, etc.<sup>5</sup> Great progress has been made in developing high-performance ASLBs. However, the battery performances of ASLBs are still dissatisfactory due to several challenges, including issues of interfacial compatibility,<sup>6</sup> structure stability,<sup>7</sup> Li dendrite suppression,<sup>8</sup> and large-scale processing.<sup>9</sup> Therefore, advanced characterizations are highly desired to reveal the underlying mechanisms in the ASLBs. Nondestructively and *operando* visualizing the reaction processes of ASLBs is regarded as one of the most

efficient methods to relate the fundamental mechanisms with the battery behaviors.<sup>10</sup> First, without extracting the sample from the battery, nondestructive characterizations eliminate the risks that the sample of interest could be damaged or contaminated, resulting in misleading conclusions. Next, *operando* investigations allow monitoring the reaction processes in the ASLBs in real time. Conventional *ex situ* characterizations generally supply discrete evidence from samples in different batches.<sup>11</sup> Because batteries usually suffer from self-discharge, the *ex situ* results are not consistent with those in the battery. Furthermore, the visualization of the ASLBs provides a chance to intuitively observe the morphology evolutions inside the ASLBs.<sup>12</sup> Considering the reactions in ASLBs are couples of chemistry, electrochemistry, and mechanics, the visualization of the ASLBs contributes to a comprehensive investigation. Therefore, developing advanced nondestructive tools for *operando* visualization is of significance in understanding the electro-chemo-mechanic reaction mechanisms in ASLBs.

In this article, for the first time, we discuss the application of neutron imaging, a representative nondestructive tool, *in*

Daxian Cao, State Key Laboratory of Pulp and Paper Engineering, Plant Fiber Research Center, School of Light Industry and Engineering, South China University of Technology, Guangzhou, People's Republic of China; Department of Mechanical and Industrial Engineering, Northeastern University, Boston, USA; dcao0714@scut.edu.cn

Yuxuan Zhang, Neutron Scattering Division, Oak Ridge National Laboratory, Oak Ridge, USA; zhangy6@ornl.gov

Tongtai Ji, Department of Mechanical and Industrial Engineering, Northeastern University, Boston, USA; ji.to@northeastern.edu

Hongli Zhu, Department of Mechanical and Industrial Engineering, Northeastern University, Boston, USA; h.zhu@neu.edu

\*Corresponding author

doi:10.1557/s43577-023-00611-7

*operando* visualizing the ASLBs. Firstly, we briefly compare various *operando* visualization tools and summarize their pros and cons in developing nondestructive visualization of ASLBs. Next, we introduce the mechanism of neutron imaging and summarize its requirements for the *operando* investigation. Following, we review the progress of neutron imaging *in operando* investigating the all-solid-state Li metal batteries (ASLMBs) and all-solid-state Li-sulfur batteries (ASLSBs). Finally, we analyze the prospect of neutron imaging in characterizing the ASLBs.

### Summary of various *operando* visualization techniques

A multitude of *operando* visualization tools, each with its distinct strengths and weaknesses, have been implemented in the characterization of ASLBs, as outlined in **Table I**. These tools can be grouped based on their spatial resolution into (1) Ultrasonic imaging<sup>13</sup> and magnetic resonance imaging (MRI),<sup>14,15</sup> which offer resolutions exceeding 100  $\mu\text{m}$ ; (2) x-ray imaging,<sup>16–22</sup> neutron imaging,<sup>23–27</sup> and optical microscopy,<sup>28–32</sup> all of which can achieve a few micrometers; (3) electron microscopies, such as scanning electron microscopy (SEM)<sup>33–37</sup> and transmission electron microscopy (TEM),<sup>38–42</sup> which are distinguished by their nanometer scale. Despite significant advancements, not all of these methods fulfill the requirements for a nondestructive *operando* visualization of ASLBs. Ultrasonic imaging and MRI, two notable nondestructive visualization tools, find extensive use in fields such as engineering and medical treatments. However, their application to ASLBs is challenged by their relatively limited spatial resolution. Typically, the interfaces in ASLBs span from nanometers to a few micrometers, which is significantly less than the hundreds of micrometers that these methods can resolve. In contrast, electron microscopies, known for their high spatial resolution in nanometers, have been effectively utilized for *in situ* or *ex situ* tracking of interfaces and reaction mechanisms. Despite their strengths, these methods require specialized sample designs and are limited to localized observation. The reactions taking place within ASLBs encompass a complex interplay of mechanical, electrical, and chemical processes. The complex reactions taking place during service are extremely difficult to replicate in *in situ* electron microscopy investigations. Furthermore, the electron beams used in these methods can potentially damage sensitive materials such as Li metal, sulfide solid electrolytes (SEs), and sulfur. Moreover, conclusions drawn from localized observation could skew the understanding of the bulk reactions within the battery. In other words, they may not fully capture the holistic behavior of these reactions, thereby leading to potential misconceptions. Therefore, although electron microscopies offer high resolution, their applicability to the comprehensive study of ASLBs is limited.

Nondestructive imaging techniques such as optical microscopy, x-ray imaging, and neutron imaging can be used to visualize the internal structure and operation of ASLBs in

real time. Optical microscopy has been reported for visualizing the Li metal behavior in ASLMBs, especially when using transparent polymer SEs.<sup>31</sup> However, optical microscopy can only observe the surface reactions in opaque ceramic-SE-based ASLBs.<sup>32</sup>

Specially designed cells are required to expose the region of interest. In comparison, x-ray imaging and neutron imaging are highlighted with high transmission ability, providing a chance for nondestructively visualizing the inner reactions in ASLBs. X-ray imaging, including x-ray tomography, has been reported with great achievement in visualizing the reactions in the ASLBs.<sup>21,43</sup> Ning et al. tracked the dendrite growth within the cracks during plating.<sup>21</sup> Lewis reported interphase growth and void generation at the Li|SE interface.<sup>22</sup> X-ray imaging shows a powerful nondestructive visualization ability for ASLBs. However, it is unfortunate that x-ray cannot tell Li metal from voids and cracks. Because Li metal reactions often generate voids, regions with low x-ray attenuation could correspond to either lithium metal or voids. In contrast, neutron imaging is advantageous for visualizing light elements such as Li in ASLBs.<sup>23</sup> Neutron imaging can be used to differentiate the Li information from the voids, getting rid of the limitation in x-ray imaging. Therefore, neutron imaging is one of the most promising visualization tools for nondestructively investigating ASLBs. However, currently, there are few works reported using neutron imaging in ASLBs, which is mainly attributed to the limited access to neutron-related techniques.

### Comparison of neutron imaging to x-ray imaging

Neutron imaging, akin to x-ray imaging (**Figure 1a**), serves as a nondestructive approach for exploring the internal features, structures, and distributions of an object in its entirety.<sup>46</sup> It leverages the distinctive interaction between neutrons and matter, enabling it to visualize contrasts complementary to those discernible through x-ray imaging.

First, due to their ability to penetrate several millimeters or even centimeters into metals, neutrons make excellent probes for studying materials housed within apparatuses designed to control factors such as temperature, pressure, or other stimuli. This high penetration depth is also applicable to radiation shielding materials, such as lead, making neutrons instrumental in characterizing irradiated materials.

Second, neutrons exhibit a heightened sensitivity to light elements (such as hydrogen, lithium, etc.), showing a stark contrast to x-rays (**Figure 1b**).<sup>47</sup> This sensitivity stems from the larger cross sections associated with these elements, which has catalyzed the development of neutron imaging as an invaluable tool in a myriad of research fields. These include energy-storage materials, additive manufacturing (AM), geology, nuclear materials, and more.

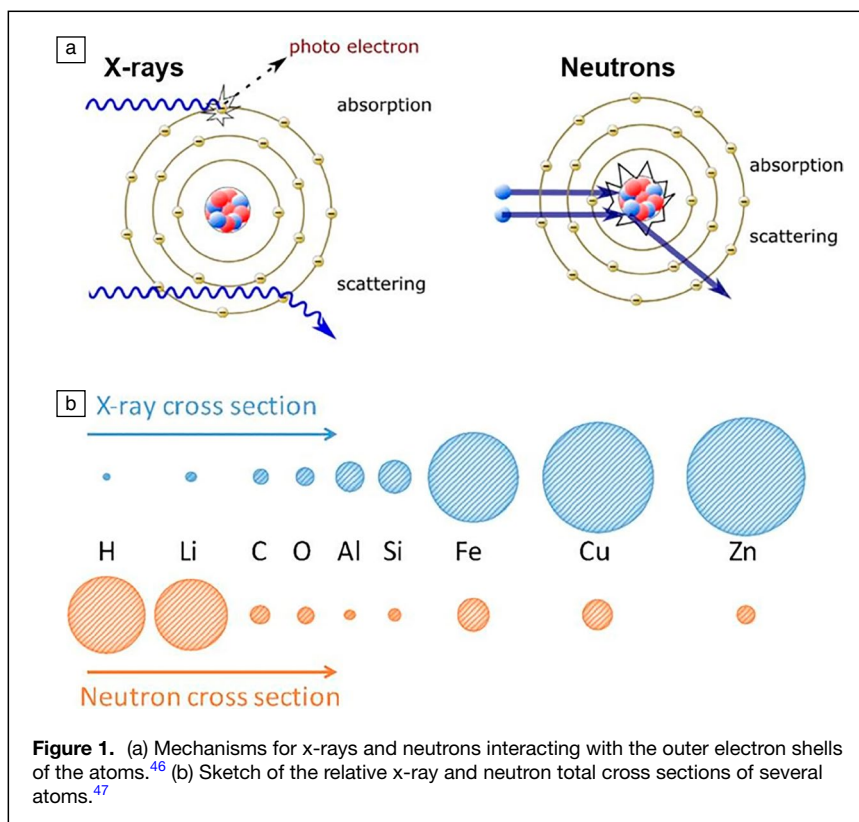
Furthermore, the sensitivity of neutrons to light elements can be adjusted by either enriching or depleting specific isotopes. For instance, isotopes such as <sup>7</sup>Li and deuterium are

Table I. Techniques for *operando* imaging characterizations used in ASLBs.

Technique	Measurement	Typical Resolution Spatial Resolution (m)	Temporal Resolution	Characterization Depth	Advantages	Limitation	References
<b>Visible light</b>							
Optical microscopy (OM)	Visible light	$10^{-7}$ – $10^{-3}$ (up to sub $\mu\text{m}$ )	1–10 s	Surface and side-view morphology	Low cost; easy operation; Direct commonly used; High time resolution; Good for transparent solid electrolyte; Can further combine with other techniques, such as Raman imaging. <sup>39</sup>	Surface characterization for untransparent materials; special cell request (window needed)	28–32
<b>Electron Beam</b>							
Scanning electron microscopy (SEM)	Backscattered electrons, secondary electrons, or x-rays	$10^{-9}$ – $10^{-4}$ (nm to $\mu\text{m}$ )	1–10 s	Surface morphology	Can further combine with other electron-beam techniques, such as auger electron spectroscopy (AES) mapping <sup>33</sup> and energy-dispersive spectroscopy. <sup>34</sup>	Surface characterization; Electronic conductivity request; Special cell with open surface request; Special sample holder request; High vacuum environment	33–37
Scanning transmission electron microscopy (STEM)	Fore-scattered electrons, transmitted electrons, or x-rays	$10^{-10}$ – $10^{-5}$ (up to atomic scale)	Few seconds	Near-surface morphology (nm to $\mu\text{m}$ )	High resolution; Can further combine with other electron-beam techniques, such as electron energy-loss spectroscopy (EELS), <sup>40</sup> and annular bright field (ABF) imaging, <sup>41</sup> differential phase contrast scanning transmission electron microscopy (DPC-STEM) (to identify space charge layer) <sup>33</sup>	Special cell design request (usually fabricated by sputtering and e-beam evaporation methods); Special sample holder request; Strict to thickness; Hard to characterize electron-beam-sensitive materials, such as metallic Li, Na, or S-based electrolytes; <sup>39</sup> High vacuum environment	39–42, 44
<b>X-ray</b>							
Imaging Transmission x-ray microscopy (TXM)	The scattering, transmission, or absorption of the x-ray	$10^{-8}$ – $10^{-4}$ (nm to $\mu\text{m}$ )	Tens of microseconds	mm	High resolution; High characterization depth; Simple <i>in situ</i> cell design with stacking pressure applied; Can further combine with other x-ray techniques, such as x-ray absorption near-edge structure; spectroscopy (XANES) <sup>17</sup>	Li metal is invisible; Hard to detect overlapped structure on the horizontal direction	16, 17

Table 1. (continued)

Technique	Measurement	Typical Resolution Spatial Resolution (m)	Temporal Resolution	Characterization Depth	Advantages	Limitation	References
Computed tomography (CT)		$10^{-8}$ – $10^{-4}$ (nm to $\mu\text{m}$ )	Few mins to tens of mins	Surface and bulk morphology	High resolution; No limit of sample size; Can explore internal 3D structure	Low time resolution; Low Li sensitivity; Hard to distinguish Li, pores, and cracks	18–22
Neutron Imaging	The scattering, transmission, or absorption of the neutron radiation	$10^{-5}$ – $10^{-4}$ (tens of $\mu\text{m}$ )	Few seconds to few mins	mm	Direct detection of lithium and lithium concentration; Isotope discriminable; High characterization depth; Simple <i>in situ</i> cell design with stacking pressure applied	Limited facilities; Hard to detect overlapped structure on the horizontal direction	23–27
Computed tomography (CT)		$10^{-5}$ – $10^{-4}$ (tens of $\mu\text{m}$ )	Few hours	Surface and bulk morphology, element distribution	Can explore internal 3D structure, map spatial distribution	Low spatial and time resolution; High cost	24–26
Neutron depth profiling (NDP)	Thermal neutrons (n) react with $^6\text{Li}$ emitting alpha particles ( $^4\text{He}$ ) and tritons ( $^3\text{H}$ )	$10^{-7}$ – $10^{-3}$ (up to sub $\mu\text{m}$ )	1–10 min	Element distribution in depth ( $\mu\text{m}$ )	Highly sensitive to lithium; Transmissive z-axis element distribution	Low sensitivity in x-y plane; High cost; Special cell design request	45
Other							
Ultrasonic testing (UT)	Acoustic waves	$10^{-4}$ – $10^{-2}$ (sub mm)	Few mins	Liquid distribution (mm)	Highly sensitive to void and gas	Low resolution	13
Magnetic resonance imaging (MRI)	Nuclear magnetic resonance signal	$10^{-4}$ (sub mm)	1–10 min	$\mu\text{m}$	Isotope discriminable $\text{Li}^0/\text{Li}^+$ discriminable	Low resolution	14, 15



**Figure 1.** (a) Mechanisms for x-rays and neutrons interacting with the outer electron shells of the atoms.<sup>46</sup> (b) Sketch of the relative x-ray and neutron total cross sections of several atoms.<sup>47</sup>

significantly less attenuating than  $^6\text{Li}$  and hydrogen, respectively. This tunability presents a significant advantage for various relevant research domains.

### Application of *operando* neutron imaging in all-solid-state Li metal batteries

The application of neutron imaging in ASLBs is currently in the initial research stage mainly due to the limited access to neutron-related techniques worldwide. Recently, it has been successfully applied in ASLMBs<sup>26,27</sup> and ASLSBs.<sup>24,25</sup> These works have demonstrated the great prospect of neutron imaging in investigating the ASLBs.

### *Operando* neutron imaging investigating the “soft short” and Li deformation in all-solid-state Li metal batteries

Li metal owns a high specific capacity ( $3860 \text{ mAh g}^{-1}$ ) and the lowest reduction potential ( $-3.04 \text{ V}$  versus standard hydrogen electrode), making it the ideal anode choice for ASLMBs.<sup>8</sup> However, ASLMBs are generally criticized for their low coulombic efficiency and poor cycling life. More severe, the Li dendrite (or called filament) can easily penetrate the SE causing a short circuit of the ASLMBs. The mechanisms of the short circuit are still debated, and advanced characterizations are highly recommended for the fundamental analysis.

The short circuit is one of the most common failures in ASLMBs. Generally, the short circuit, also called “hard short,” refers to the permanent connection of the cathode and anode inside the battery, and the battery exhibits a continuous voltage

drop-off. Meanwhile, there is another phenomenon that the battery cannot be normally charged to the set cutoff voltage and the voltage dynamically maintains stable. This phenomenon is called the “soft short,” different from the aforementioned “hard short.” The “soft short” is frequently observed in ASLMBs, but lacks deep investigations. Wang et al.<sup>48</sup> reported using cyclic voltammetry and electrochemical impedance spectra to diagnose the “soft short” in the symmetric cell. However, the mechanism for the “soft short” in ASLMBs is still unclear.

Our group used neutron imaging to *operando* investigate the “soft short” in the ASLMBs (Figure 2).<sup>26</sup> The ASLMB was a full cell comprised of an argyrodite-type sulfide SE, Li metal anode, and  $\text{LiNi}_{0.8}\text{Mn}_{0.1}\text{Co}_{0.1}\text{O}_2$ -based cathode. Figure 2a shows the 2D neutron radiograph image of the ASLMB. The Li-containing components displayed dark gray color. Along the axial direction as the arrow shows, the transmission distribution in the marked box is plotted in Figure 2b. The stainless-steel (SS)-made current collector, cathode, SE, and Li metal anode layers were

well distinguished according to the transmission differences related to the Li concentration. Therefore, the transmission fluctuation can be employed to monitor the Li concentration evolution in real time. The transmission change ratio,  $\text{Tr}_t/\text{Tr}_0$ , was utilized to further amplify the transmission change during the battery test, where  $\text{Tr}_0$  and  $\text{Tr}_t$  represent the transmissions at the beginning and at the charging time  $t$ , respectively, as illustrated in Figure 2c. The fluctuation of the transmission change ratio and corresponding colors can well display the Li concentration evolution: if  $\text{Tr}_t/\text{Tr}_0 > 1$ , the Li concentration is reduced, and the region was marked with bright color; if  $\text{Tr}_t/\text{Tr}_0 < 1$ , the trend was reversed; if  $\text{Tr}_t/\text{Tr}_0 = 1$ , it showed Viridis color representing no Li concentration change. Because the neutron transmission depth in regions at the middle and edge are different, two regions of interest marked with Region I and Region II were selected for *operando* observation (Figure 2d). As shown in Figure 2e, the ASLMB showed a typical “soft short” failure after charging for 4.5 h. Then the voltage dynamically maintained stable, but not kept rising or dropping off. Figure 2f displayed the real-time evolution of the  $\text{Tr}_t/\text{Tr}_0$  at Region I. The colors present the Li transmission change: color more toward blue means Li depletion ( $\text{Tr}_t/\text{Tr}_0 > 1$ ); color more toward red represents Li enrichment ( $\text{Tr}_t/\text{Tr}_0 < 1$ ); green color depicts no Li change ( $\text{Tr}_t/\text{Tr}_0 = 1$ ). The Li evolution in cathode, anode, and interface were well displayed. Before the “soft short,” the cathode layer (marked as P1) displayed a Li depletion, and the anode|SE interface (P2) showed Li enrichment, attributed to the delithiation of the  $\text{LiNi}_{0.8}\text{Mn}_{0.1}\text{Co}_{0.1}\text{O}_2$  and Li



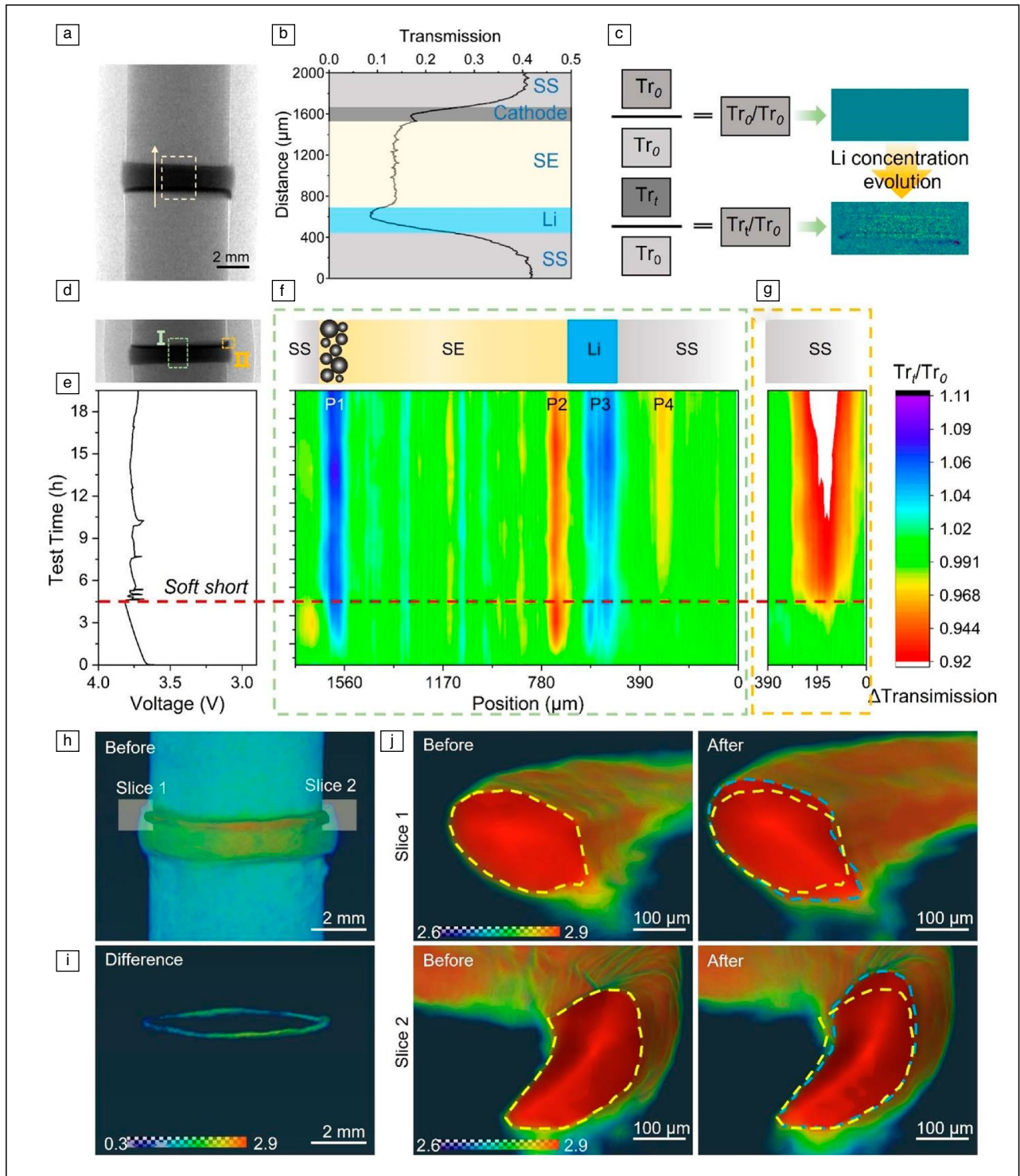


**Figure 2.** Operando neutron imaging investigating the “soft short” and Li deformation in all-solid-state Li metal batteries (ASLMBs).<sup>26</sup> (a) Two-dimensional neutron radiograph of the ASLMB before test, and (b) the neutron transmission profile along the arrow direction in the marked box. (c) The logic for transmission data treatment. (d) Radiograph of the ASLMB as prepared. Two boxes demonstrate two regions of interest. (e) Galvanostatic charge profile of the ASLMB to show the “soft short.” The intensity mapping of the real-time transmission changes at the regions with (f) green box and (g) orange box. (h) Three-dimensional tomography images of the ASLMB before the battery test and (i) the attenuation increment. (j) Zoom-in tomography images to show the morphology evolution before (left) and after (right) at slice 1 and slice 2 marked in (h). The outlines of Li are highlighted with yellow and blue dashed lines. SE, solid electrolyte; SS, stainless steel.

plating, respectively. After the “soft short,” the Li concentration in the cathode and anode fluctuated, consistent with the battery voltage. An x-ray computed tomography scan was conducted to record the SE morphology after the “soft short.” The Li metal within cracks partially penetrates the SE. Therefore, fluctuations of the voltage, as well as the Li concentration in the cathode, were mainly attributed to the dynamic connection and disconnection between the cathode and the anode.

Note that there was a Li depletion layer at the anode|SS interface (P3) and a Li enhancement at the SS (P4), which were attributed to the deformation of Li. There was no distraction from the SS at Region II, therefore the Li enrichment at the P4 position was more prominent (Figure 2g).

Notably, when the ASLMB was in “soft short,” the Li concentration at the cathode side fluctuated while the one at the anode side, especially at P4, continued to accumulate, strongly confirming that faradic reactions still occurred.

Besides the *operando* 2D neutron imaging, the *ex situ* 3D CT of the ASLMB before and after the electrochemical test was conducted to record the spatial evolution. Figure 2h shows the reconstructed 3D structure of the ASLMB before the test. The 3D structure of the ASLMB was well displayed. After the reaction, the 3D structure of the ASLMB was also built, and the Li concentration enhancement can be extracted with a subtraction treatment (Figure 2i). A Li enrichment at the anode side was observed. For more details, the two slices (Figure 2h) were employed to extract the cross-section morphology of the Li, and the outlines of the Li were highlighted with dashed lines, as shown in Figure 2j. There was Li expansion in the top and bottom, while a shrink in the middle region, consisting of the Li accumulation and depletion layers at P2 and P3, respectively. The Li expansion to the top region contributed to the Li deformation.

In summary, in a nondestructive manner, neutron imaging can not only *operando* monitor the Li concentration evolutions through 2D radiography, but also track the spatial change through the *ex situ* 3D CT. Different from the “hard short,” the ASLMB in “soft short” showed evidence for the faradic reactions. Meanwhile, there was Li deformation observed. This study elucidates the crucial role of external pressure in mitigating the growth of dendrites, which can subsequently result in dendrite fractures. This provides key insights into the genesis of both “soft” and “hard” shorts in Li metal batteries.

### Li dynamics in mixed ion–electron conducting interlayer

Introducing an ion-conducting interlayer to separate the Li metal and the SE is regarded as an effective way to suppress the dendrite growth. An ideal interlayer is demanded with high ionic conductivity, electron insulation, stability against  $\text{Li}^0$  and SE, high mechanical strength, and less porosity. LiPON is a promising candidate,<sup>49</sup> but needs complex sputtering deposition, limiting its applications. Other reported interlayers, such as polymer electrolytes,<sup>50</sup>  $\text{Li}_3\text{N-LiF}$ ,<sup>51</sup> carbon-Ag,<sup>52</sup> and graphite,<sup>53</sup> cannot meet all requirements. In particular, the

carbon-Ag and graphite interlayers are excellent electron conductors, and the reported batteries delivered record-breaking performances. It seems that electron insulation is not necessary for the interlayer when using these mixed ionic-electronic conductors (MIECs).

Our group developed *operando* neutron imaging to reveal the Li dynamics inside the ASLMBs, especially at the graphite-made MIEC interlayer.<sup>27</sup> Figure 3a illustrated the mechanochemistry and mechano-electrochemistry processes in the battery assembly and electrochemical measurement. This ASLMB was designed as a full cell coupling  $\text{LiNi}_{0.8}\text{Mn}_{0.1}\text{Co}_{0.1}\text{O}_2$ -based cathode, an argyrodite-type sulfide SE, Li metal anode, and a thin graphite interlayer between the SE and Li metal. During the densifying process, graphite spontaneously reacts with the Li metal under mechanical pressure, resulting in forming of the Li-graphite interlayer. Raman and x-ray diffraction revealed that the Li-graphite was composed of  $\text{LiC}_6$ , diluted graphite intercalated compound, and Li metal. Then as the ASLMB was charged, Li migrated from cathode to anode and mainly plated at the interface between SE and Li-graphite, resulting in the dendrite growth followed by the short circuit. The result was contradictory to the expectation. Advanced characterization was desired to reveal the Li behavior, and thus *operando* neutron imaging was employed.

Figure 3b displayed the 2D neutron radiograph image of the ASLMB, which showed a layered structure. Similarly, the neutron transmission distribution along the axial direction can be used to identify the interfaces between adjacent layers (Figure 3c). Then the transmission change ratio  $\text{Tr}_t/\text{Tr}_0$  was utilized to evaluate the Li concentration evolution. This ASLMB failed after being charged for 180 min, and then the voltage dropped to a low value quickly, demonstrating a “hard short.” Figure 3c lists the time-stamped images after the transmission data treatment mentioned in Figure 3b. The fluctuation of the transmission change ratio and corresponding colors can well display the Li concentration evolution: if  $\text{Tr}_t/\text{Tr}_0 > 1$ , the Li concentration is reduced, and the region was marked with bright color; if  $\text{Tr}_t/\text{Tr}_0 < 1$ , the trend was reversed; if  $\text{Tr}_t/\text{Tr}_0 = 1$ , it showed gray color representing no Li concentration change. Before the short circuit, there was a pair of Li accumulation and depletion layers observed, and the intensities were gradually enhanced. When the battery was charged to 180 min, the dark and bright spots gradually disappeared simultaneously.

Because the contrast in the image was not high enough, the transmission intensity mapping was used to give more information (Figure 3d). The colors present the Li transmission change: color more toward blue means Li depletion ( $\text{Tr}_t/\text{Tr}_0 > 1$ ); color more toward red represents Li enrichment ( $\text{Tr}_t/\text{Tr}_0 < 1$ ); green color depicts no Li change ( $\text{Tr}_t/\text{Tr}_0 = 1$ ). Overall, the cathode layer showed Li depletion and the anode layer was enriched with Li. More specifically, there were three stages during the charging process. At Stage I (0–90 min), Li migrated from the cathode and mainly deposited at the interface between the Li-graphite and the SE, and no signal for Li was deposited inside or beneath the Li-graphite. This

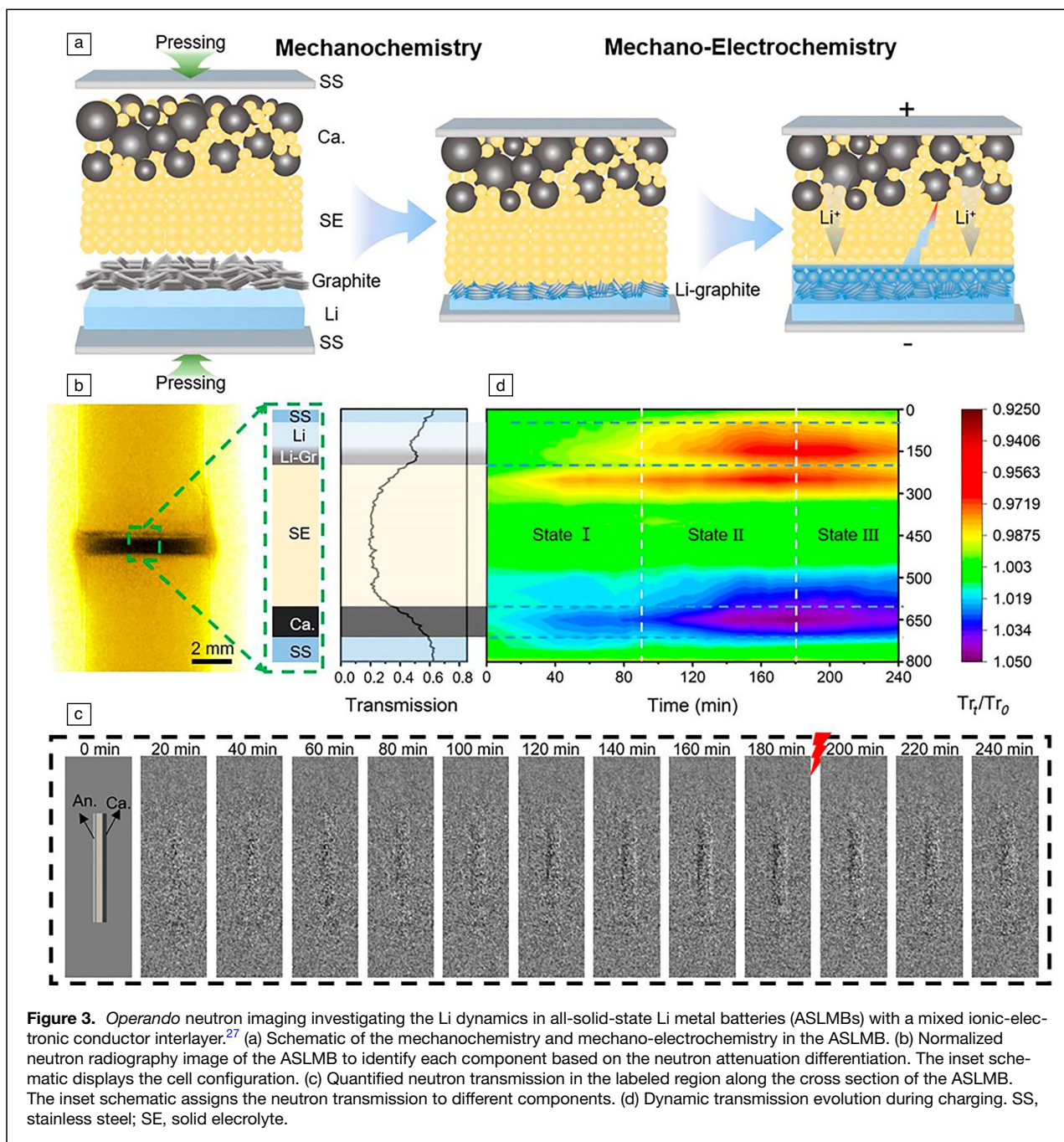


**Figure 3.** *Operando* neutron imaging investigating the Li dynamics in all-solid-state Li metal batteries (ASLMBs) with a mixed ionic-electronic conductor interlayer.<sup>27</sup> (a) Schematic of the mechanochemistry and mechano-electrochemistry in the ASLMB. (b) Normalized neutron radiography image of the ASLMB to identify each component based on the neutron attenuation differentiation. The inset schematic displays the cell configuration. (c) Quantified neutron transmission in the labeled region along the cross section of the ASLMB. The inset schematic assigns the neutron transmission to different components. (d) Dynamic transmission evolution during charging. SS, stainless steel; SE, solid electrolyte.

demonstrated that Li preferred to deposit onto graphite, but not transport across the Li-graphite layer. Then at Stage II (90–180 min), the Li concentration continued to increase at the Li-graphite|SE interface, as well as started to accumulate inside the Li-graphite and initial Li metal regions, demonstrating the Li-ion can transport across the Li-graphite interlayer after the saturation in the interlayer in Stage II. In the final Stage III, the ASLMB experienced an internal short circuit, as indicated by the Li concentration shifting from the anode side to the cathode region. The reason is the Li dendrite penetrated the SE causing a direct connection between Li metal and the cathode. All of these evidences proved that *operando* neutron

imaging was an ideal tool for nondestructively visualizing the reaction inside the ASLMBs. As previously mentioned, neutron-based techniques are incapable of differentiating between Li metal and Li ions. Given that graphite can also intercalate with Li ions, it is not straightforward to attribute the accumulation of Li within the Li-graphite interlayer at Stage II to Li metal deposition alone. Therefore, we integrated *operando* Raman spectroscopy to analyze the Li behaviors within the Li-graphite interlayer. This is because the graphite's intercalation and the deposition of Li metal onto the graphite can be distinctly identified via Raman spectroscopy. The results demonstrated a preference for Li to deposit onto, rather than



intercalate into, the graphite. This deposition preference is triggered by the saturated edges and the enhanced disorder occurring during the mechanochemical process.

In summary, neutron imaging is powerful to nondestructively monitor the Li concentration evolution in the ASLMB benefiting the reaction mechanism investigation. To comprehensively analyze the behavior of Li, including Li metal and Li ions, incorporating other advanced techniques is highly recommended. This work proved that a promising MIEC interlayer needs to have the lowest nucleation barrier at the  $\text{Li}^0$  side to drive the  $\text{Li}^+$  to transport across MIEC and preferentially deposit onto the  $\text{Li}^0$ .

### The application of neutron imaging in all-solid-state Li sulfur batteries

Bradbury and colleagues<sup>24</sup> utilized neutron imaging to explore the rate-limiting step in all-solid-state Li sulfur (Li-S) batteries. They designed a specific cell encased in aluminum with a polyimide sleeve, depicted in **Figure 4a**. The materials used for the cathode, solid electrolyte, and anode were S/C/Li<sub>6</sub>P-S<sub>5</sub>Cl, Li<sub>6</sub>PS<sub>5</sub>Cl, and In-Li, respectively. Given the varying neutron absorption coefficients of different materials, the neutron beam's attenuation differed as it passed through the cell. These signals were detected and used to form a neutron image. In the context of all-solid-state Li-ion batteries, Li—possessing the highest neutron absorption coefficient—is the only significantly mobile element during the electrochemical cycling process. Hence, the change in the neutron beam's attenuation is closely tied to Li's movement, enabling the tracking of Li behavior in ASLSBs.

**Figure 4b** presents *operando* neutron images of the ASLSBs at different depths of discharge (DoD). To emphasize the dynamics of Li transport through the cathode composite, the rate of change in neutron attenuation was calculated and represented in the neutron images. It's evident that the “reaction front,” exhibiting the maximum rate of attenuation, advances from the separator (solid electrolyte) side toward the current collector during discharge. Neutron tomography can be employed to create a 3D representation of the cell and highlight Li's spatial distribution, as illustrated in **Figure 4c**. By subtracting the pristine state from the fully discharged and charged states, the Li distribution alteration throughout the cell can be visualized. The anode shows a negative attenuation change due to Li loss, and the separator displays zero net change given the stable Li concentration in the solid electrolyte. At the fully discharged state, the augmented Li concentration in the composite sulfur cathode indicates Li<sub>2</sub>S formation. At the recharged state, the cathode area's Li concentration remains higher than the pristine state, implying that Li<sub>2</sub>S isn't entirely reverted to S—a phenomenon linked to capacity loss. More specifically, Li distribution within the cathode is heterogeneous, as portrayed in the right plot of **Figure 4c**.

Notably, the charged cathode's attenuation change peak is closer to the current collector (higher “*d*”) than the discharged

cathode. This difference (green plot) signifies the mobile Li transported back to the anode during charging, predominantly lost from the cathode's solid electrolyte separator side. **Figure 4d** presents the attenuation change in neutron tomography slices from  $d_0$  to  $d_{\text{max}}$  at the fully discharged and recharged states.

Using the data obtained from neutron imaging and extending the conventional “1D porous electrode theory,” also known as the Newman model, to solid-state sulfur cathodes, Bradbury and colleagues delved deeper into the reaction fronts' phenomenon and transport limitations in the ASLSB. They found that when a cathode composite's effective ionic and electronic conductivities are inadequate, the reaction current becomes nonuniform. If the effective electronic conductivity surpasses ion conductivity, the reaction front migrates from the separator side to the current collector side, in line with the experimental findings. Conversely, an electron-transport limited reaction front will transition from the current collector side to the solid electrolyte side when the ionic conductivity is considerably higher than electronic conductivity. A capacity loss mechanism was revealed from the reaction front propagation phenomenon. As the reaction front shifts from the separator side to the current collector side, the composite's effective ionic conductivity diminishes, thus impeding further delithiation from the current collector side.

### Summary and outlook

This article focused on the application of neutron imaging, a nondestructive tool, for *operando* visualization of ASLBs. The advantages and limitations of various *operando* visualization techniques are discussed, including ultrasonic imaging, magnetic resonance imaging (MRI), x-ray imaging, electron microscopy, and optical microscopy. Among these techniques, neutron imaging stands out as a promising tool due to its high sensitivity to light elements such as lithium.

The article presented the progress of neutron imaging *in operando* investigations of ASLMBs and ASLSBs. In ASLMBs, neutron imaging has been used to study the “soft short” phenomenon and the deformation of Li metal. It allows for the real-time visualization of Li concentration evolution and provides insights into the failure mechanisms. In ASLSBs, neutron imaging has been employed to analyze the rate-limiting step and Li dynamics during discharge and charge processes. The visualization of reaction fronts and Li distribution helps to understand the transport limitations and capacity loss in ASLSBs. Neutron imaging has emerged as a powerful nondestructive tool for *operando* visualization of ASLBs. Its unique sensitivity to light elements, such as Li, allows for the real-time monitoring of Li concentration evolution and provides valuable insights into the reaction mechanisms and failure modes of ASLBs. However, the application of neutron imaging in ASLBs is still in the early stages, mainly due to limited access to neutron-related techniques.

In the future, it is expected that neutron imaging will play a more significant role in the characterization of ASLBs.

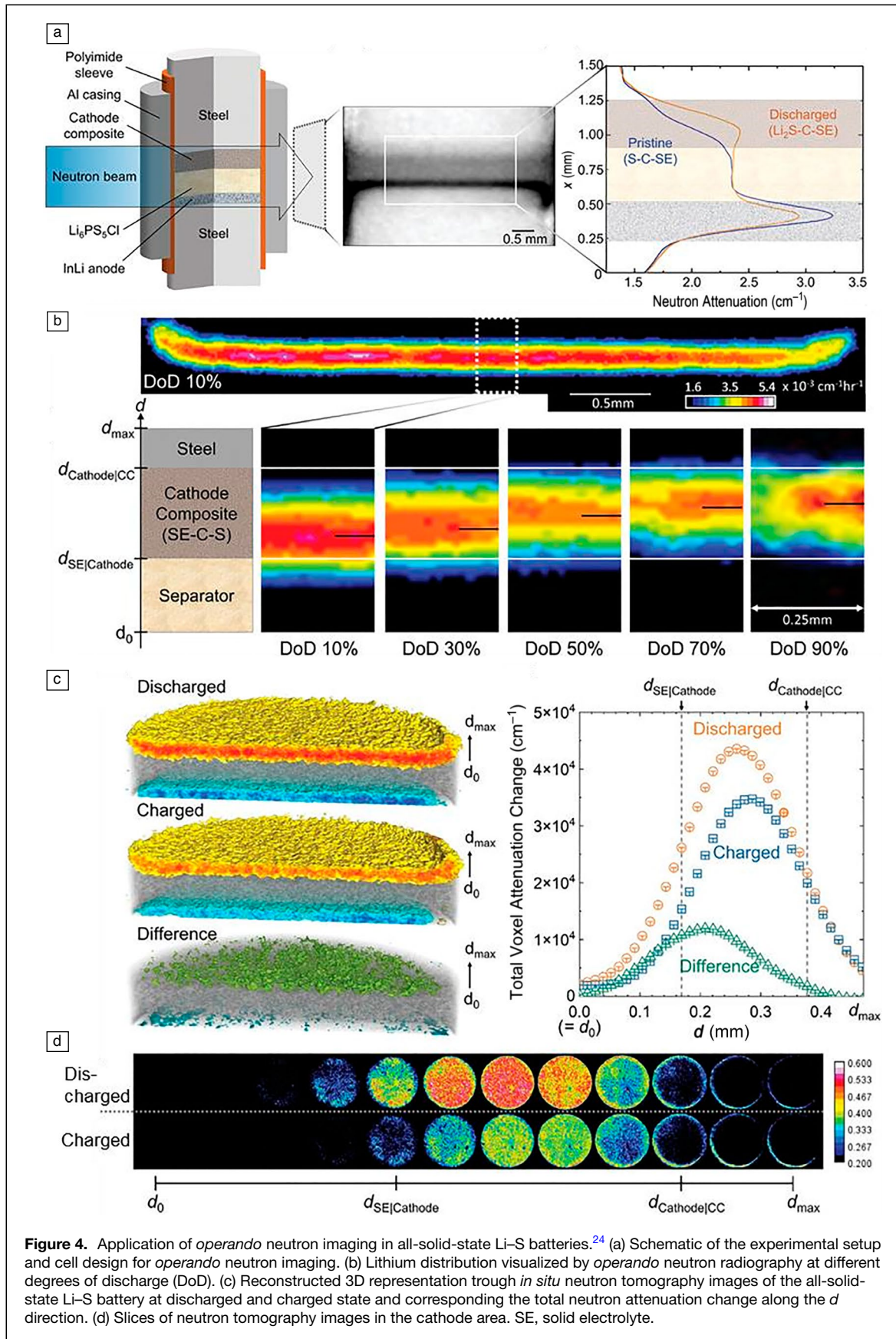


**Figure 4.** Application of *operando* neutron imaging in all-solid-state Li-S batteries.<sup>24</sup> (a) Schematic of the experimental setup and cell design for *operando* neutron imaging. (b) Lithium distribution visualized by *operando* neutron radiography at different degrees of discharge (DoD). (c) Reconstructed 3D representation through *in situ* neutron tomography images of the all-solid-state Li-S battery at discharged and charged state and corresponding the total neutron attenuation change along the  $d$  direction. (d) Slices of neutron tomography images in the cathode area. SE, solid electrolyte.

Advances in neutron imaging technology, such as improved spatial resolution and faster acquisition times, will enable more detailed and comprehensive investigations of ASLBs. Furthermore, efforts should be made to expand the application of neutron imaging to other types of ASLBs, beyond ASLMBs and ASLSBs, to gain a broader understanding of the challenges and opportunities in the field. Overall, neutron imaging holds great promise as a valuable tool for the development and optimization of ASLBs. By providing nondestructive, real-time visualization of ASLBs, neutron imaging can contribute to the advancement of battery technologies, leading to safer and higher-performing energy-storage systems for electric vehicles and other applications.

### Acknowledgments

This research used resources at the High Flux Isotope Reactor, a DOE Office of Science User Facility operated by the Oak Ridge National Laboratory. H.Z. acknowledges financial support from NSF- CBET-ES (1924534) and the DOE Basic Energy Science DE-SC0024528. H.Z. acknowledges the financial support received from the Office of Science Department of Energy under Award No. DE-SC0024528.

### Funding

Open access funding provided by Northeastern University Library.

### Data availability

Not applicable.

### Conflict of interest

On behalf of all authors, the corresponding author states that there is no conflict of interest.

### Open Access

This article is licensed under a Creative Commons Attribution 4.0 International License, which permits use, sharing, adaptation, distribution and reproduction in any medium or format, as long as you give appropriate credit to the original author(s) and the source, provide a link to the Creative Commons licence, and indicate if changes were made. The images or other third party material in this article are included in the article's Creative Commons licence, unless indicated otherwise in a credit line to the material. If material is not included in the article's Creative Commons licence and your intended use is not permitted by statutory regulation or exceeds the permitted use, you will need to obtain permission directly from the copyright holder. To view a copy of this licence, visit <http://creativecommons.org/licenses/by/4.0/>.

### References

1. International Energy Agency (IEA), *Global EV Outlook* (IEA, Paris, 2020)
2. Y.-K. Sun, *ACS Energy Lett.* **5**, 3221 (2020)
3. J. Janek, W.G. Zeier, *Nat. Energy* **8**, 230 (2023)

4. Q. Zhang, D. Cao, Y. Ma, A. Natan, P. Aurora, H. Zhu, *Adv. Mater.* **31**, 1901131 (2019)
5. P. Albertus, V. Anandan, C. Ban, N. Balsara, I. Belharouak, J. Buettner-Garrett, Z. Chen, C. Daniel, M. Doeff, N.J. Dudney, B. Dunn, S.J. Harris, S. Herle, E. Herbert, S. Kalnaus, J.A. Libera, D. Lu, S. Martin, B.D. McCloskey, M.T. McDowell, Y.S. Meng, J. Nanda, J. Sakamoto, E.C. Self, S. Tepavcevic, E. Wachsman, C. Wang, A.S. Westover, J. Xiao, T. Yersak, *ACS Energy Lett.* **6**, 1399 (2021)
6. S. Lou, F. Zhang, C. Fu, M. Chen, Y. Ma, G. Yin, J. Wang, *Adv. Mater.* **33**, 2000721 (2021)
7. X.-D. Zhang, F.-S. Yue, J.-Y. Liang, J.-L. Shi, H. Li, Y.-G. Guo, *Small Struct.* **1**, 2000042 (2020)
8. D. Cao, X. Sun, Q. Li, A. Natan, P. Xiang, H. Zhu, *Matter* **3**, 57 (2020)
9. D. Cao, Y. Zhao, X. Sun, A. Natan, Y. Wang, P. Xiang, W. Wang, H. Zhu, *ACS Energy Lett.* **5**(11), 3468 (2020). <https://doi.org/10.1021/acseenergylett.0c01905>
10. J. Scharf, M. Chouchane, D.P. Finegan, B. Lu, C. Redquest, M.-C. Kim, W. Yao, A.A. Franco, D. Gostovic, Z. Liu, M. Riccio, F. Zelenka, J.-M. Doux, Y.S. Meng, *Nat. Nanotechnol.* **17**, 446 (2022)
11. Y. Xiang, X. Li, Y. Cheng, X. Sun, Y. Yang, *Mater. Today* **36**, 139 (2020)
12. B. Chen, H. Zhang, J. Xuan, G.J. Offer, H. Wang, *Adv. Mater. Technol.* **5**, 2000555 (2020)
13. H. Huo, K. Huang, W. Luo, J. Meng, L. Zhou, Z. Deng, J. Wen, Y. Dai, Z. Huang, Y. Shen, *ACS Energy Lett.* **7**, 650 (2022)
14. P.-H. Chien, X. Feng, M. Tang, J.T. Rosenberg, S. O'Neill, J. Zheng, S.C. Grant, Y.-Y. Hu, *J. Phys. Chem. Lett.* **9**, 1990 (2018)
15. X. Liu, Z. Liang, Y. Xiang, M. Lin, Q. Li, Z. Liu, G. Zhong, R. Fu, Y. Yang, *Adv. Mater.* **33**, 2005878 (2021)
16. J. Charbonnel, N. Darmet, C. Deilhes, L. Broche, M. Reyrier, P.-X. Thivel, R. Vincent, *ACS Appl. Energy Mater.* **5**, 10862 (2022)
17. S. Lou, Q. Liu, F. Zhang, Q. Liu, Z. Yu, T. Mu, Y. Zhao, J. Borovilas, Y. Chen, M. Ge, X. Xiao, W.-K. Lee, G. Yin, Y. Yang, X. Sun, J. Wang, *Nat. Commun.* **11**, 5700 (2020)
18. Y. Kimura, M. Fakkao, T. Nakamura, T. Okumura, N. Ishiguro, O. Sekizawa, K. Nitta, T. Uruga, M. Tada, Y. Uchimoto, *ACS Appl. Energy Mater.* **3**, 7782 (2020)
19. N. Sun, Q. Liu, Y. Cao, S. Lou, M. Ge, X. Xiao, W.K. Lee, Y. Gao, G. Yin, J. Wang, *Angew. Chem.* **131**, 18820 (2019)
20. S. Hao, S.R. Daemi, T.M. Heenan, W. Du, C. Tan, M. Storm, C. Rau, D.J. Brett, P.R. Shearing, *Nano Energy* **82**, 105744 (2021)
21. Z. Ning, D.S. Jolly, G. Li, R. De Meyere, S.D. Pu, Y. Chen, J. Kasemchainan, J. Ihli, C. Gong, B. Liu, D.L.R. Melvin, A. Bonnin, O. Magdysyuk, P. Adamson, G.O. Hartley, C.W. Monroe, T.J. Marrow, P.G. Bruce, *Nat. Mater.* **20**, 1121 (2021)
22. J.A. Lewis, F.J.Q. Cortes, Y. Liu, J.C. Miers, A. Verma, B.S. Vishnugopi, J. Tippens, D. Prakash, T.S. Marchese, S.Y. Han, C. Lee, P.P. Shetty, H.-W. Lee, P. Shevchenko, F. De Carlo, C. Saldana, P.P. Mukherjee, M.T. McDowell, *Nat. Mater.* **20**, 503 (2021)
23. R.F. Ziesche, N. Kardjilov, W. Kockelmann, D.J.L. Brett, P.R. Shearing, *Joule* **6**, 35 (2022)
24. R. Bradbury, G.F. Dewald, M.A. Kraft, T. Arit, N. Kardjilov, J. Janek, I. Manke, W.G. Zeier, S. Ohno, *Adv. Energy Mater.* **13**(17), 2203426 (2023). <https://doi.org/10.1002/aenm.202203426>
25. R. Bradbury, N. Kardjilov, G.F. Dewald, A. Tenggattini, L. Helfen, W.G. Zeier, I. Manke, *Adv. Funct. Mater.* **33**(38), 2302619 (2023)
26. D. Cao, K. Zhang, W. Li, Y. Zhang, T. Ji, X. Zhao, E. Cakmak, J. Zhu, Y. Cao, H. Zhu, *Adv. Funct. Mater.* 2307998 (2023)
27. D. Cao, Y. Zhang, K. Burch, M. Geiwitz, J. Bilheux, K. Xu, Q. Tu, H. Zhu, Revealing Li dynamics in mixed ionic-electronic conducting interlayer of all-solid-state batteries, Preprint, *ChemRxiv* (2022). <https://chemrxiv.org/engage/chemrxiv/article-detail/6331b19ee615023c7d275203>
28. W. Guo, F. Shen, J. Liu, Q. Zhang, H. Guo, Y. Yin, J. Gao, Z. Sun, X. Han, Y. Hu, *Energy Storage Mater.* **41**, 791 (2021)
29. M. Otoyama, Y. Ito, A. Hayashi, M. Tatsumisago, *J. Power Sources* **302**, 419 (2016)
30. G. Feng, H. Jia, Y. Shi, X. Yang, Y. Liang, M.H. Engelhard, Y. Zhang, C. Yang, K. Xu, Y. Yao, W. Xu, X. Shan, *Nat. Nanotechnol.* **18**, 780 (2023)
31. C. Brissot, M. Rosso, J.N. Chazalviel, S. Lascaud, *J. Power Sources* **81-82**, 925 (1999)
32. E. Kazyak, M.J. Wang, K. Lee, S. Yadavalli, A.J. Sanchez, M.D. Thouless, J. Sakamoto, N.P. Dasgupta, *Matter* **5**, 3912 (2022)
33. K.N. Wood, K.X. Steirer, S.E. Hafner, C. Ban, S. Santhanagopalan, S.-H. Lee, G. Teeter, *Nat. Commun.* **9**, 2490 (2018)
34. H. Marceau, C.-S. Kim, A. Paoletta, S. Ladouceur, M. Lagacé, M. Chaker, A. Vijn, A. Guerfi, C.M. Julien, A. Mauger, M. Armand, P. Hovington, K. Zaghbi, *J. Power Sources* **319**, 247 (2016)
35. T. Fuchs, J. Becker, C.G. Haslam, C. Lerch, J. Sakamoto, F.H. Richter, J. Janek, *Adv. Energy Mater.* **13**, 2203174 (2023)
36. N.G. Yadav, N. Folastre, M. Bolmont, A. Jamali, M. Morcrette, C. Davoisne, *J. Mater. Chem. A* **10**, 17142 (2022)
37. Q. Li, T. Yi, X. Wang, H. Pan, B. Quan, T. Liang, X. Guo, X. Yu, H. Wang, X. Huang, L. Chen, H. Li, *Nano Energy* **63**, 103895 (2019)
38. L. Wang, R. Xie, B. Chen, X. Yu, J. Ma, C. Li, Z. Hu, X. Sun, C. Xu, S. Dong, T.-S. Chan, J. Luo, G. Cui, L. Chen, *Nat. Commun.* **11**, 5889 (2020)
39. Y. Cheng, L. Zhang, Q. Zhang, J. Li, Y. Tang, C. Delmas, T. Zhu, M. Winter, M.-S. Wang, J. Huang, *Mater. Today* **42**, 137 (2021)



40. Y. Nomura, K. Yamamoto, T. Hirayama, E. Igaki, K. Saitoh, *ACS Energy Lett.* **5**, 2098 (2020)
41. S.D. Findlay, R. Huang, R. Ishikawa, N. Shibata, Y. Ikuhara, *Microscopy* **66**(1), 3 (2017)
42. Z. Wang, D. Santhanagopalan, W. Zhang, F. Wang, H.L. Xin, K. He, J. Li, N. Dudney, Y.S. Meng, *Nano Lett.* **16**, 3760 (2016)
43. J.A. Lewis, F.J.Q. Cortes, M.G. Boebinger, J. Tippens, T.S. Marchese, N. Kondekar, X. Liu, M. Chi, M.T. McDowell, *ACS Energy Lett.* **4**, 591 (2019)
44. L. Wang, R. Xie, B. Chen, X. Yu, J. Ma, C. Li, Z. Hu, X. Sun, C. Xu, S. Dong, *Nat. Commun.* **11**, 5889 (2020)
45. C. Chen, J.F.M. Oudenhoven, D.L. Danilov, E. Vezhlev, L. Gao, N. Li, F.M. Mulder, R.-A. Eichel, P.H.L. Notten, *Adv. Energy Mater.* **8**, 1801430 (2018)
46. A. Tengattini, N. Lenoir, E. Andó, G. Viggiani, *Geomech. Energy Environ.* **27**, 100206 (2021)
47. Y. Zhang, *Study of Li-Mg alloy and Si powder anodes for Li-ion batteries: Experiments, neutron imaging and modeling* (The University of Utah, Salt Lake City, 2016), p. 108
48. C. Wang, T. Deng, X. Fan, M. Zheng, R. Yu, Q. Lu, H. Duan, H. Huang, C. Wang, X. Sun, *Joule* **6**, 1770 (2022)
49. D. Cheng, T.A. Wynn, X. Wang, S. Wang, M. Zhang, R. Shimizu, S. Bai, H. Nguyen, C. Fang, M.-C. Kim, W. Li, B. Lu, S.J. Kim, Y.S. Meng, *Joule* **4**(11), 2484 (2020)
50. C. Wang, K.R. Adair, J. Liang, X. Li, Y. Sun, X. Li, J. Wang, Q. Sun, F. Zhao, X. Lin, R. Li, H. Huang, L. Zhang, R. Yang, S. Lu, X. Sun, *Adv. Funct. Mater.* **29**, 1900392 (2019)
51. X. Ji, S. Hou, P. Wang, X. He, N. Piao, J. Chen, X. Fan, C. Wang, *Adv. Mater.* **32**, 2002741 (2020)
52. Y.-G. Lee, S. Fujiki, C. Jung, N. Suzuki, N. Yashiro, R. Omoda, D.-S. Ko, T. Shiratsuchi, T. Sugimoto, S. Ryu, J.H. Ku, T. Watanabe, Y. Park, Y. Aihara, D. Im, I.T. Han, *Nat. Energy* **5**, 299 (2020)
53. L. Ye, X. Li, *Nature* **593**, 218 (2021) □

**Publisher's note**

Springer Nature remains neutral with regard to jurisdictional claims in published maps and institutional affiliations.



**Daxian Cao** is an associate professor in the School of Light Industry and Engineering and State Key Laboratory of Pulp and Paper Engineering at South China University of Technology (SCUT), China. Prior to joining SCUT, he worked as a postdoctoral research associate at Northeastern University from 2019 to 2023. He received his PhD degree in electrical engineering from Xi'an Jiaotong University, China, in 2019. His current research interests include all-solid-state batteries, advanced characterizations, and high-value applications of the biomass. Cao can be reached by email at [dcao0714@scut.edu.cn](mailto:dcao0714@scut.edu.cn).



**Yuxuan Zhang** is the lead instrument scientist at the Multimodal Advanced Radiography Station (MARS), High Flux Isotope Reactor (HFIR) beamline (CG-1D) at Oak Ridge National Laboratory. He received his PhD degree in metallurgical engineering from The University of Utah in 2016. His research focuses on applying advanced neutron imaging techniques in the fields of materials science (such as energy-storage material, advanced nuclear materials, and additive manufacturing). Zhang can be reached by email at [zhangy6@ornl.gov](mailto:zhangy6@ornl.gov).



**Tongtai Ji** is a doctoral candidate in the Department of Mechanical and Industrial Engineering at Northeastern University. He received his bachelor's degree in materials science and engineering from Southwest Jiaotong University, China, in 2017. His master's degree was obtained from Northeastern University in 2020. His research areas include all-solid-state batteries and flow batteries. Ji can be reached by email at [ji.t@northeastern.edu](mailto:ji.t@northeastern.edu).



**Hongli Zhu** is an associate professor at Northeastern University, and co-directs their Advanced and Intelligent Manufacturing Program. Her group focuses on electrochemical energy storage, sustainable biomass-derived materials, and advanced manufacturing. Previously, she researched nanocellulose at the University of Maryland and sustainable biomaterials at Sweden's KTH Royal Institute of Technology. Specializing in energy storage, her team delves into solid-state batteries, flow batteries, and various alkali metal-ion batteries. Recognized in *Advanced Materials* and *ACS Energy Letters*, she has 17,500+ citations and an H-index of 63. Awards include the Søren Buus Outstanding Research Award and Northeastern University College of Engineering Faculty Fellow. Zhu can be reached by email at [h.zhu@neu.edu](mailto:h.zhu@neu.edu).